

Rapid Frequency-Domain FLIM Spinning Disk Confocal Microscope: Lifetime Resolution, Image Improvement and Wavelet Analysis

Chittanon Buranachai · Daichi Kamiyama ·
Akira Chiba · Benjamin D. Williams · Robert M. Clegg

Received: 12 August 2007 / Accepted: 29 January 2008 / Published online: 7 March 2008
© Springer Science + Business Media, LLC 2008

Abstract A spinning disk confocal attachment is added to a full-field real-time frequency-domain fluorescence lifetime-resolved imaging microscope (FLIM). This provides confocal 3-D imaging while retaining all the characteristics of the normal 2-D FLIM. The spinning disk arrangement allows us to retain the speed of the normal 2-D full field

FLIM while gaining true 3-D resolution. We also introduce the use of wavelet image transformations into the FLIM analysis. Wavelets prove useful for selecting objects according to their morphology, denoising and background subtraction. The performance of the instrument and the analysis routines are tested with quantitative physical samples and examples are presented with complex biological samples.

C. Buranachai
Center of Biophysics and Computational Biology,
University of Illinois, Urbana-Champaign,
1110 W Green St, Loomis Lab,
Urbana, IL 61801, USA
e-mail: chittanon.buranachi@gmail.com

D. Kamiyama · A. Chiba
Department of Biology, University of Miami,
1301 Memorial Drive,
Coral Gables, FL 33124, USA

D. Kamiyama
e-mail: daichi.kamiyama@gmail.com

A. Chiba
e-mail: akira-chiba@miami.edu

B. D. Williams
Cell & Struc Biology,
University of Illinois, Urbana-Champaign,
601 S Goodwin, M/C 123,
Urbana, IL 61801, USA
e-mail: bdwillms@life.uiuc.edu

R. M. Clegg (✉)
Department of Physics,
University of Illinois, Urbana-Champaign,
1110 W Green St, Loomis Lab,
Urbana, IL 61801, USA
e-mail: rclegg@uiuc.edu

Keywords FLIM · FLI · Lifetime imaging · Spinning Disk · Microscope · Polar plot · Wavelet · Morphology · Background subtraction · Denoising

Introduction

FLIM (FLI)

Fluorescence lifetime-resolved imaging microscopy (FLIM or just FLI) combines micrometer spatial resolution of fluorescence imaging with nanosecond temporal resolution of fluorescence lifetimes. Since the fluorescence lifetime is a characteristic of a fluorophore in a given environmental condition, *in vitro* cuvette type measurements have been used extensively to distinguish different fluorescence species even when their emission spectra are closely overlapped, or to probe differences in molecular environments of the fluorophores [1, 2]. Despite the usefulness of lifetime information, the cuvette type measurements contain no spatial information. FLIM provides researchers a unique tool that increases the contrast of the image by taking advantage of different fluorescence lifetimes. Two examples

of the discriminate powers of FLIM are detecting heterogeneities in samples [3] and localizing in an image the effects of specific analytes on fluorescence lifetimes [4, 5]. However, the most general application of FLIM, especially in live cell imaging, is imaging Förster Resonance Energy Transfer (FRET). Intensity based FRET imaging measurements require the determination of several parameters and corrections of artifacts, such as the donor and the acceptor quantum yields, the spectral crosstalk between two channels, the direct excitation of the acceptor, etc. In contrast, FLIM (lifetime measurements in general) does not require these corrections. FLIM-based FRET is a highly reliable way to image the FRET efficiency *in vivo* [6–8].

Time and frequency domain measurements

FLIM is performed either in the time-domain or in the frequency-domain. They are Fourier transforms of each other; therefore, the information derived from both is fundamentally equivalent [9]. However, the instrumentation setups are different and in practice which method is preferable depends on the samples being measured, the required data acquisition speed and resources available [6, 10].

Time domain

In the time-domain, the time-decay fluorescence response of sharp excitation pulses (FWHM in a range of tens of femtoseconds to a few nanoseconds [2]) is measured. This is usually done by time-correlated single-photon counting (TCSPC) methods [1, 11] or by analog detection using gated delay time detection [12, 13]. The time-domain lifetime measurement concept is easy to visualize (simply the decay of fluorescence following a short excitation pulse) and it has been widely applied in both the scanning mode (either the two-photon excitation [14–16] or one-photon confocal excitation [17]), and in full field excitation, where every point in the field of view is excited simultaneously.

Frequency domain

In the frequency-domain, which is the method of measurement discussed in this paper, the frequency dispersion of the time decay of the fluorophore to a repetitive excitation light modulation at a radio frequency ω is measured (ω is the radial frequency, $\omega=2\pi f$, where f is the repetition frequency). For the sake of simplicity, only a sinusoidal excitation $E(t)$ is discussed (Fig. 1), but any high frequency repetitive signal composed of multiple harmonics can be used [9]. The fluorescence emission ($F(t)$, Fig. 1) from a sample excited with a sinusoidal excitation has the same modulation frequency ω as the excitation light. But a level of demodulation M and phase shift Φ_F of the fluorescence

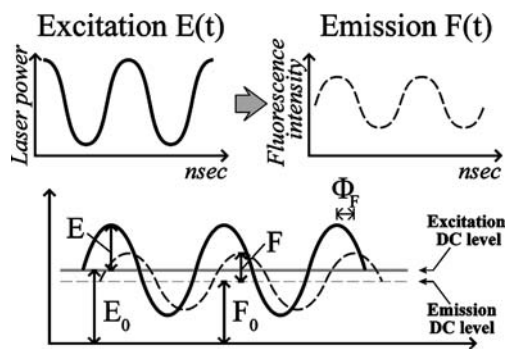


Fig. 1 Lifetime measurement in the frequency-domain. A repetitive modulated sinusoidal form of excitation light $E(t)$ is used to excite the sample, and the modulated fluorescence emission $F(t)$ is acquired in the homodyne mode for full-field excitation, or in the heterodyne mode for point scanning (see text). Lifetimes are calculated from the phase shift Φ_F and modulation ratio M , defined in Fig. 1 and Eqs. 1 and 2

are different from that of the excitation light. The values of M and Φ_F depend on the corresponding fluorescence lifetime as described by Eqs. 1 and 2 and Fig. 1.

$$M = \frac{F/F_0}{E/E_0} = \frac{1}{\sqrt{1 + (\omega\tau_M)^2}} \tag{1}$$

$$\tan \Phi_F = \omega\tau_\phi \tag{2}$$

E_0 and F_0 are the time average values of the excitation light and the fluorescence. E and F are the amplitudes of the corresponding time dependent signals. Because M and Φ_F at high frequencies (10–100 MHz) are difficult to measure, noisy and expensive, we employ a homodyne method to drastically lower the frequency response of our detection system. The homodyne method is more convenient for lifetime imaging [6] than a similar technique, called the heterodyne method, which is widely used in cuvette type lifetime measurements (a single channel detector). For details about heterodyne and homodyne method, see [9]. In the homodyne procedure the amplification gain $D(t)$ of the detector is modulated at exactly the same frequency ω as the modulated fluorescence emission (Eq. 3 and Fig. 2),

$$D(t) = D_0 + D \cdot \cos(\omega t - \Phi_D). \tag{3}$$

The output signal from the detector is averaged over a period of time T long compared to $1/\omega$. The DC result of this averaging, S_{avg} is in (Eq. 4),

$$\overline{S(\Delta\Phi_{DE})} S_{avg} = \langle F(t) \cdot D(t) \rangle = S_0 \left(1 + \frac{M}{2} \cdot \cos(\Delta\Phi_{DE} - \Phi_F) \right) \tag{4}$$

where $\Delta\Phi_{DE} = \Phi_E - \Phi_D$.

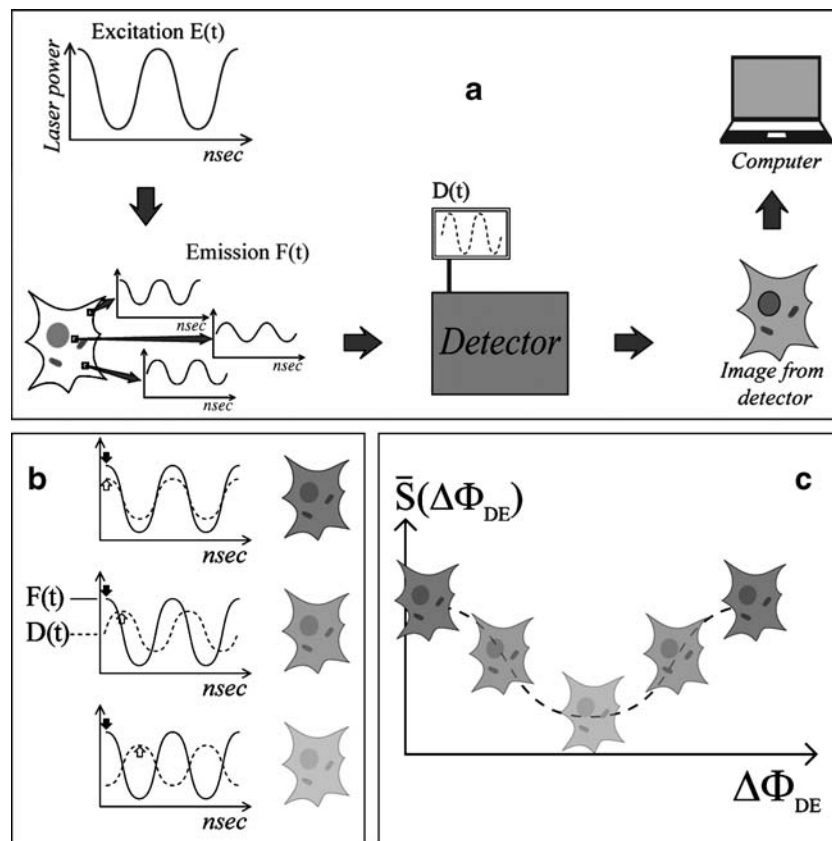


Fig. 2 (a) A diagram explaining the homodyne technique applied to full-field frequency-domain FLIM. Fluorescence emission from every point in the field of view is collected by the image intensifier whose amplification gain $D(t)$ is modulated at the same excitation modulation frequency ω but with a certain preset phase delay. (b) The high frequency fluorescence signal $F(t)$ (solid line) detected by the detector is multiplied by the amplification gain $D(t)$ (dashed line) of the

detector, preset at a given phase delay and averaged over a long period of time $T (T \gg 1/\omega)$. The intensity of images on the right of the graphs represent the level of DC signal after averaging $\bar{S}(\Delta\Phi_{DE})$, Eq. 4). (c) The output signal S_{avg} from this multiplication and average is a DC signal and is a function of the phase difference $\Delta\Phi_{DE}$. The information of M and Φ_F is preserved in $\bar{S}(\Delta\Phi_{DE})$ and can be obtained by using the digital Fourier transformation or a least square fitting method

In our current full-field FLIM setup, a gain-modulated image intensifier is the primary detector. The phosphor screen on the intensifier averages out fast components and the brightness of phosphorescence signal S_{avg} at the output port represents the DC component in fluorescence signal (Eq. 4). The demodulation M and phase shift Φ_F is obtained by collecting intensity images (S_{avg} images) at different phase offset $\Delta\Phi_{DE}$ of the detector amplification (Fig. 2 and Eq. 4).

Confocality

Accurate depth localization and reduction of out-of-focus fluorescence is critical, especially for samples with highly localized fluorescent morphologies. For instance, *in vivo*, the natural proteins to which the fluorescent proteins are hybridized usually have specific locations in the living cells where they assemble. It is often important to acquire 3-D resolved images in order to locate these targeted sites.

With our non-confocal, full field, frequency-domain FLIM setup discussed above, the data acquisition/display

can be very fast (video rates). Nevertheless, out of focus fluorescence is a problem with thick specimens using non-confocal, full-field image acquisition. 3-D resolution of objects can be obtained by acquiring a z-stack of separate images; however, this requires extensive deconvolution, which is time-consuming and is often not practical with live samples. Scanning two-photon excitation FLIM [15, 18, 19] and scanning confocal one-photon excitation FLIM [17, 20] acquire directly 3-D images; however a scanning FLIM experiment requires relatively long acquisition times (longer than we require for many of our projects) and often two photon-excitation increases the rate of photo-damage to the region inside the focal point [21].

In order to limit the out-of-focus background fluorescence without severely sacrificing the speed of data acquisition, as would be the case for single-beam scanning, we take advantage of the parallelism and the confocality provided by a spinning disk confocal head (model CSU-10, Yokogawa Corp. of America, GA) and incorporate it into our full-field FLIM setup [22]. A similar instrument has

recently been reported [23]. This improvement greatly reduces the out-of-focus fluorescence, and yet retains the speed of acquisition, which is often critical in applications such as live cell and tissue imaging.

Wavelets

We also introduce a new method of data analysis using wavelet procedures to pre-select locations of the images before the FLIM analysis is carried out. This is an excellent way to select particular morphologies in an image, as well as reduce, and often eliminate, background fluorescence based on morphology. It is frequently difficult or impossible to measure a true background image when imaging biological systems. Therefore, as a crude estimate, the background is often simply estimated from some part of the image and subtracted from a recorded image. But this is not satisfactory if the background is not constant across the image, or if it is relatively large. The wavelets provide a way to distinguish background based on a morphological character, and this will work even if the background is large. Background can arise due to scattering, unbound fluorophores or intrinsic fluorophores in samples; it is often spatially diffuse compared to the interesting locations in an image. Even though FLIM is able to distinguish locations based on the fluorescence lifetime, better results are often obtained if background can be subtracted—even with confocal images. And wavelets present an effective and convenient way to accomplish this. We have found it valuable for distinguishing fine structures out of background in fluorescence images of living cells expressing fluorescent proteins, before we carry out the FLIM data analysis.

Materials and methods

Spinning disk confocal FLIM

We have incorporated a spinning disk confocal head (model CSU-10, Yokogawa Corp. of America, GA) into our full-field FLIM setup. The CSU-10 converts an expanded single excitation laser beam into approximately one thousand miniature beams. These are focused through pinholes in a spinning disk onto the sample by the microscope objective lens. The focal points of the multiple excitation points are progressively scanned over the sample as the spinning disk rotates. The pinholes in the disk are arranged in a constant pitch spiral pattern. A rotation of 30° completes a full raster scanning of the excitation grid over the field of view. Therefore, with a rotation rate of 30 Hz, 360 confocal quality images are collected. For more technical details of the CSU-10,

refer to [24]. Such high speed data acquisition is not possible with a single beam confocal scanning microscope. The spinning disk setup can be used for rapid dynamic image acquisition *in vivo* [25]. The instrumentation setup for our spinning disk FLIM is shown in Fig. 3.

An Ar⁺ laser (Model 2213, Cyonics Uniphase, CA) is the light source and a Pockel's cell (Model: 350-105, Conoptics Inc, CT) modulates the excitation light. The laser is coupled into a single mode optical fiber (Point Source, Southampton, U.K.), which on the other end is connected to the input port of a CSU-10 spinning disk head (Fig. 3 inset). The excitation beam illuminates a selected region on the multi-microlens disk, covering about 1,000 microlenses. Each lens focuses the beam passing the dichroic mirror onto a corresponding pinhole on the pinhole disk. The addition of the microlens disk (Yokogawa design [26]) in front of the pinhole disk increases the excitation light to about 40–60% of the input, instead of 1% otherwise [27]. The pinhole disk is designed to be at the optical conjugate plane to the microscope's objective focal plane [24]. The excitation beams are refocused by the tube lens and the objective lens onto the sample. Fluorescence emitted from the sample is collected and focused onto the same set of pinholes. As a result, each pinhole is used twice—for excitation and emission. The in-focus fluorescence reflects off the dichroic mirror and is focused onto the image intensifier (HRI, Kentech Instrument, Oxfordshire, UK). The position of the illuminated microlenses and the pinholes constantly change

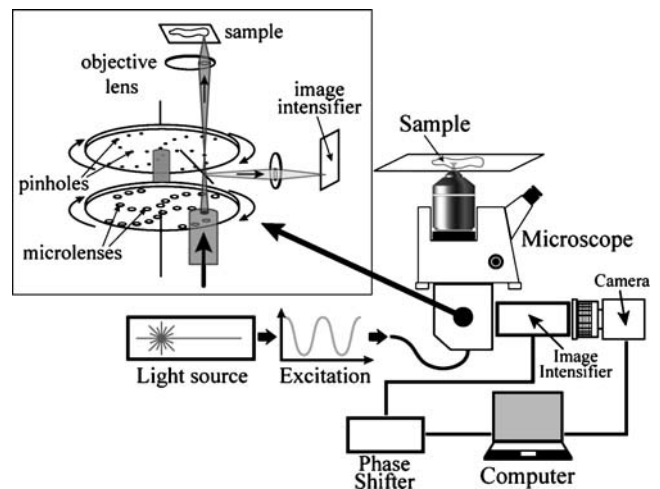


Fig. 3 Spinning disk fluorescence lifetime confocal microscopy in the frequency-domain. The extra part being added to the conventional setup is a spinning disk confocal module (*inset*, model CSU-10, Yokogawa Corp. of America, GA). Because the period of time a focused laser beam traverse across a diffraction limited spot on the sample is much longer than the period of excitation modulation, the two requirements of the homodyne techniques mentioned in the text are still valid. See text for more detail

while the disks are spinning, resulting in the raster scanning of the excitation points on the sample and the corresponding points on the image intensifier. On the image intensifier, each pixel “sees” the fluorescence signal intermittently during the scanning. The time it takes an excitation beam to sweep the diffraction limited spot will be the on-time the excitation passes a microlens. An on-time of $\sim 100 \mu\text{s}$ as reported by Wang et al. [28] is much longer than the period of the high frequency light modulation (10 ns at a modulation repetition frequency of $f=100 \text{ MHz}$). Therefore, the requirements for a homodyne measurement are met, and the system can be treated as a conventional full-field FLIM experiment (see the “Supplementary Data” for details). The phase-shift is performed on the emission side. The sinusoidal signal (synthesized from a signal generator HP 8657A) is passed through a 9-bit digital phase-shifter (Lorch Microwave, Salisbury, MD) prior to being amplified and used to drive the cathode voltage of the image intensifier. The phase is shifted over a full 2π period with an even number N of equal steps. A reference PMT is used to monitor the drift in the performance of the Pockel’s cell (not shown in Fig. 3). The fluctuation in the laser power is corrected by normalizing the raw images with the reference images taken periodically from a reference phase.

Data acquisition and data analysis and presentation are carried out by custom-made software written in Microsoft’s Visual C++ (Microsoft Inc., OR) with the Measurement Studio plug-in (National Instrument, TX), Matlab (The Mathworks, Inc., MA) and OriginPro (OriginLab Corp., MA).

Data analysis and presentation

The polar plot

The polar plot analysis [29–31] is a convenient and information-rich display of the FLIM data. This is a plot of $M \sin(\Phi_F)$ vs $M \cos(\Phi_F)$. The polar plot is a common way to present data arising from frequency-domain measurements, such as dielectric dispersion data [32–34]. When used in FLIM, measured phase and modulation values are uniquely displayed as points on the polar plot. There are multiple benefits of the polar plot analysis: (1) it is model free, (2) the polar plot values from a single lifetime component, or a sum of several components, are uniquely located on the plot and can be promptly distinguished, and (3) the combination of multiple lifetimes is a weighed sum of the fractional intensities (the fraction of the total measured intensity that is derived from each lifetime component). For more information of the benefits of the polar plot analysis on the FLIM data, please refer to [29, 30].

After correcting for phase offsets by using a lifetime image standard (e.g. fluorescein in 0.1 M NaOH with a

known single lifetime of 4.1 ns [35]) and fitting Eq. 4 to the homodyne signal using the Fourier analysis [36], every pixel contains three numerical values: the average intensity I , the phase shift Φ_F and the modulation M . On the polar plot, the x -axis and the y -axis correspond to $M \cos(\Phi_F)$ and $M \sin(\Phi_F)$, respectively. If a single decaying lifetime component is present, the point on the polar plot will lie on a semicircle centered on the x -axis at $x=0.5$, with a radius of 0.5; faster single lifetimes lie further in a clockwise direction on the semicircle. Multiple lifetimes will lie inside the semicircle. Double lifetime components will lie on a straight line between the two single lifetime locations on the semicircle.

Wavelets

The wavelet transform is a multi-scale analysis scheme. There are many different wavelet methods and transforming functions [37, 38]. Wavelets can be used for 1-, 2- and 3-D data. In imaging it is most often used for denoising [39, 40], denoising before later image processing [41], image compression [42–44], location of dominant effects in an image [45] edge detection [46] and for object detection before particle tracking [47]. Wavelet transforms extract features within an image by selective filtering of localized space/scale characteristics of images. It is a way to detect spatial frequency characteristics of image data at a local scale rather than a global scale. The more familiar 2-D Fourier image analysis reports on spatial frequencies in an image on a global scale and the transform is a function of frequency only. Windowed Fourier transformation of images tries to analyze localized regions of images, but suffers from drastic edge effects, and the transform is still only a function of the spatial frequency [48]. Wavelet transformations have units of space and frequency (scale). Low precision in spatial localization correlates with high precision of the low frequency scale components, and high precision in the spatial localization (high spatial frequencies) correlates with low precision in the frequency (scale) dispersion. Wavelets are generalized local basis functions that can be stretched (dilated) and translated with a flexible resolution in both space and frequency. For each wavelet function the dilation property sets the spatial extent, and the translation property locates the position of the wavelet application within the image.

We use multi-resolution image decomposition wavelets to select features of interest and to eliminate background fluorescence in FLIM images. The analysis involves two sets of localized functions: a scaling function and an associated wavelet function. As described by Mallat [37], the scaling function can be seen as a low-pass filter, whereas the wavelet is similar to a band-pass filter. By passing the image data through a series of dilated wavelets

together with the associated scaling functions, the analysis acts similar to a “filter bank” [49]. As the image data is iterated through the image filter bank, the wavelet algorithm selects morphologies in the image with scales of successively narrower spatial frequency band-pass and lower spatial resolution (less detail), decomposing the original image into multi resolution “approximation” and “detail” coefficient matrices. Using all the coefficients derived through this process, the original image can be recreated exactly by applying the inverse wavelet transform. The low pass image at some iteration of wavelet/scaling procedure will be an image that has been “denoised” (of high frequencies). The differences between two low pass scaled images selects the morphologies in the image with spatial frequencies in the differential bandpass region. Using the coefficients in this spatial frequency bandpass, the inverse transform creates an image with the selected morphologies (corresponding to the selected localized spatial frequencies). This image is then used for the FLIM analysis. We have found this very useful; not only for denoising, but in selecting localized morphologies in live cells images, and in removing background fluorescence that exhibits very different morphologies than the interesting part of the image.

The wavelet analysis is performed by a set of functions in Matlab’s Wavelet Toolbox 4 (The Mathworks, Inc., MA) based on a dyadic scale using biorthogonal wavelets (bior 3.7). Following the selection of the structures in the image selected on the basis of morphology (Figs. 5 and 9), the edited image is analyzed with our custom FLIM analysis software and presented on a polar plot (Fig. 9).

Results and discussion

Performance of spinning disk confocal FLIM

Temporal performance: Fluorescein mixed with KI

The ability of the spinning disk FLIM to report accurate lifetimes is verified by measuring the fluorescence lifetime of fluorescein solution placed in a microcuvette at different concentrations of KI (a fluorescence quencher) as shown in Figs. 4a,b. The fluorescein has one lifetime that decreases as KI dynamic quenching takes place. As the concentration of the KI increases, the lifetime decreases and the points move in a clockwise fashion on the semicircle, towards faster times [30]. Because the fluorescence decays predominantly as a single component, the points are distributed in a symmetrical fashion about a point on the semicircle (Fig. 4a). The symmetrical cluster of points for every measurement is due to random noise in the low intensity pixels. In Fig. 4a, a point in a cluster represents a fit for M

and Φ_F of a single pixel in a given FLIM data set. In this case (all lifetimes should be the same) the accuracy of the fit can be improved considerably by increasing signal-to-noise (higher excitation intensity) and/or averaging the points over many pixels before fitting the FLIM data. For lower signal-to-noise images of cellular fluorescence, Gaussian weighted averaging of several pixels surrounding each separate pixel, rather than just linear averaging, is recommended to diminish the probability of artifacts due to outliers [50].

Temporal and spatial performance: fluorescence beads

To further verify the ability of the setup to measure accurately fluorescence lifetimes in conjunction with confocality, the FLIM measurements of 0.2 μm polystyrene fluorescence beads (Molecular Probes, Invitrogen, CA) were carried out; the results are shown in Fig. 4b. The beads are prominently displayed in the intensity image and well distinguished above background in the FLIM images (especially the modulation values). As expected, the lifetimes are the same regardless of the intensities of the beads. Even though the confocal intensity image clearly shows the beads above the background, if the background is not subtracted the FLIM algorithm will attempt a fit of Φ_F and M values in the areas between the beads. If the fluorescence intensity is low in these areas, these Φ_F and M values will have correspondingly larger errors, and will probably deviate from the Φ_F and M in the beads, even if the same fluorophore is in these background regions as in the beads.

Some of this light in the background areas (between the beads) can arise from reflections of the fluorescence from the beads off the surface of the microscope slide and from scattering of the bead fluorescence from the material surrounding the beads; this scattering is low, especially with confocal measurements, but will have the same lifetime as direct fluorescence from the beads. On the other hand, this scattering is common when measuring non-confocal FLIM with biological samples. Also, some excitation light could leak through the optical dichroic/filter combination, and this will contribute a component with a modulation and phase.

Including these areas in the FLIM analysis and display will deteriorate the quality of the total FLIM image. If one wants to determine the fluorescence lifetime in the separate beads, a way to select the bead structure must be found. Wavelets can be used for this.

Examples of wavelet performance

In order to further reduce the background and also help selecting the region of interest, we utilized wavelet analysis on the data.

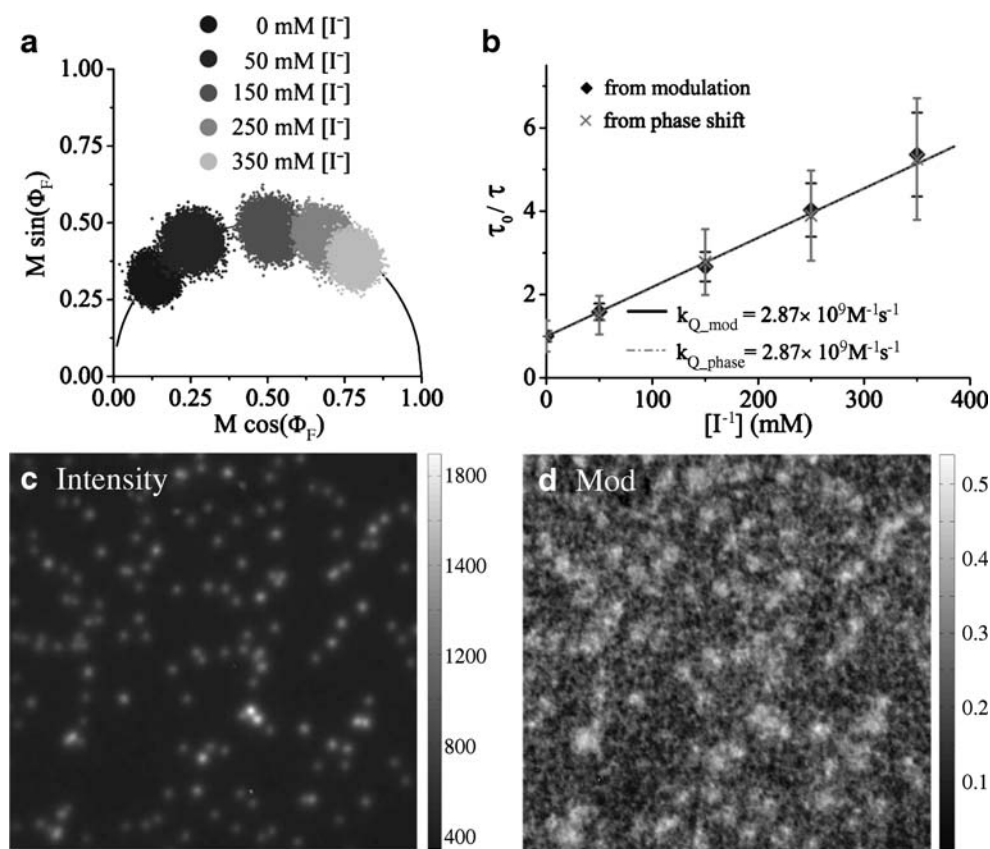


Fig. 4 Data taken with the spinning disk confocal FLIM setup. **(a)** The polar plot analysis of FLIM data from a set of fluorescein solutions having different concentrations of iodide, which quenches the fluorescence emission from fluorescein in diffusion controlled encounters. The reduction in a single fluorescence lifetime resulting from the increase in $[I^-]$ can be described as $\tau = 1/(k_0 + k_Q[I^-])$ [2]. The points at every concentration of $[I^-]$ are clustered about points on the semi-circle line, consistent with single lifetime values. The quencher is present at a large excess compared to fluorescein at every point of measurements, except the first point. At 0 mM $[I^-]$, the lifetime of fluorescein is 4.1 ns under the given conditions. As expected from the iodide quenching reaction, the Stern–Volmer plot

[2] in **(b)** yields a diffusion limited bimolecular quenching constant, calculated from the modulation lifetime (k_{Q_mod}) and from the phase shift lifetime (k_{Q_phase}). **(c, d)** FLIM data from fluorescence beads. The sample consists of 0.2 μm fluorescent beads (Molecular Probes, Invitrogen) immobilized on a glass surface in T50 (10 mM Tris+ 50 mM NaCl pH 8.0). In the confocal intensity image **(c)**, the beads are well separated from the background. The beads are clearly seen in the FLIM demodulation image **(d)**. But there is still background interference accompanying the low fluorescence. The background has not been subtracted from the image data before the FLIM fit is made, and no low intensity clipping has been made

Fluorescence images of fluorescent beads

Figure 5a is the original image and Fig. 5b is after wavelet application. Figure 5a and b demonstrate the capability of the wavelet analysis to select features of interest in the bead data and to reduce background. In both Fig. 5a and b, a 10% threshold is set relative to the maximum in each image (that is, the lower 10% intensity pixels are blanked out). The light colored boundaries designate the boundaries of this threshold, and are not part of the intensity data set. In Fig. 5b, the broad background fluorescence (with low spatial frequencies) has been subtracted by the wavelet application. This is a convenient way to automatically select objects with certain morphologies in an image for

further analysis. For instance, the fluorescence lifetime information can then be fitted only from the bead locations selected by the wavelet application (e.g. see also the discussion of Fig. 9). We are investigating the expediency of such an application to analyze automatically large sets of FLIM microarray data where the morphology in each microarray spot is to be selected based on morphology before the FLIM analysis (unpublished data).

Fluorescence images of dendrites in a *Drosophila melanogaster* larva

Figure 5c and d show a similar wavelet application on an image of dendrites in a *D. melanogaster* larva expressing

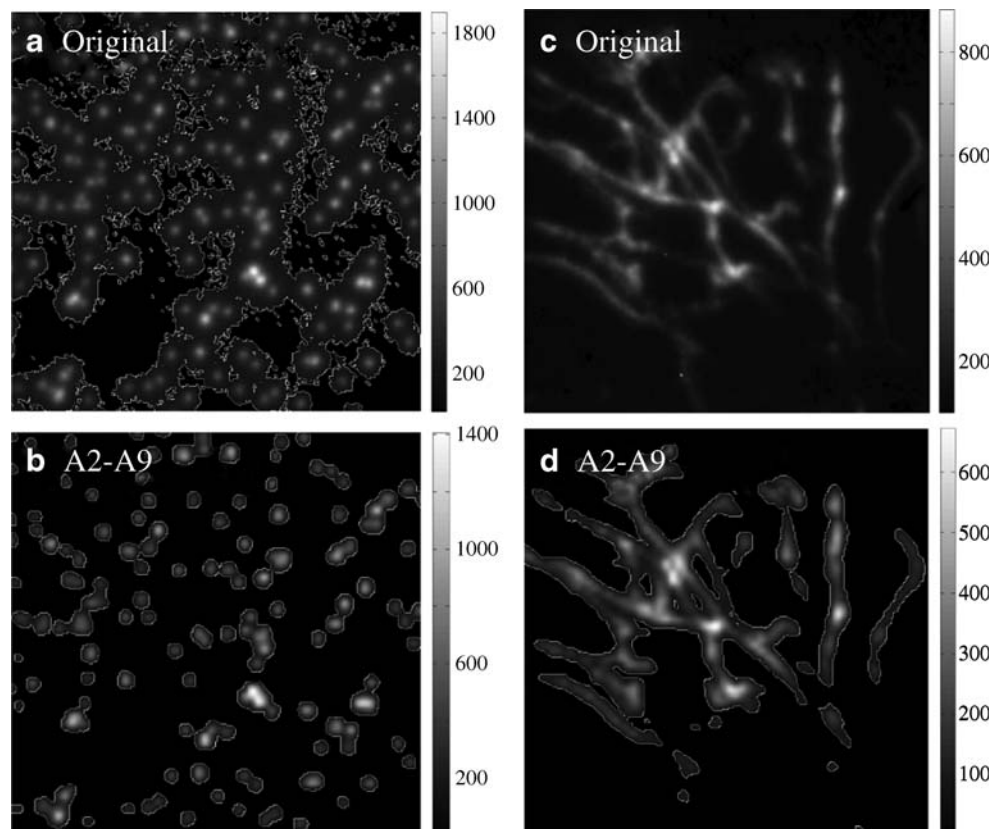


Fig. 5 Background subtraction using wavelet on the fluorescent beads image (**a** and **b**) and on the dendrites in a *D. melanogaster* larva expressing membrane-tagged GFP (**c** and **d**). The original images (**a** and **c**) and the edited image analyzed with wavelet (**b** and **d**) are compared. The region of interest is selected based on 10% peak-intensity threshold. On the bottom (**b** and **d**), the original images are decomposed by the ‘*wavedec2*’ function using Matlab Wavelet Toolbox, and the final images are reconstructed by the ‘*wrcoef2*’

function from the difference in the approximation data level 2 (containing both high and low spatial frequency components) and level 9 (containing mostly low spatial frequency component). As can be seen, after the rejection of low spatial frequency components in wavelet, which is from the background fluorescence, most of the signal left in the image is from the fluorescent beads (**b**) and from the dendrites (**d**), which contribute mainly to high spatial frequency components of the image

membrane-tagged GFP. In this case the wavelet filtering selects regions of interest involving the continuous fibril structure of the dendrites in addition to the more localized fluorescent spots within the extended structure. If the threshold of the wavelet filtered image is increased, the more highly localized areas are then primarily selected (not shown). By choosing different levels of wavelet iterations, different wavelet functions, and different thresholds *after* the wavelet application, different structures can be selected for further analysis. For instance in Fig. 5d, raising the threshold will progressively emphasize the high intensity spots, and deemphasize the fibrils. In some instances, when the images have drastically different intensities between the structures of interest and background, it may be that simple thresholding on the original image suffices. However, the wavelet transform selects regions based on local spatial frequencies and morphology *before* the thresholding is performed. Therefore, even larger background intensities, as well as high random noise, are deemphasized through the

wavelet bandpass filtering. And this is done on a local scale. Thus most of the background is subtracted from the image by the wavelet transform. In the data of Fig. 5c and d this property is useful to retain the fibril structure for further analysis. The direct benefit of the wavelet analysis on FLIM data will be discussed later when discussing the data in Fig. 9.

Spinning disk FLIM with and without wavelets: simulated lifetime images

Next we demonstrate the use of wavelets for subtracting background. This is a valuable addition to FLIM besides de-noising and to the selection of regions of interest in images. The idea is to use the multi-resolution image decomposition on every phase-delayed image in order to individually remove the signal from locations with low frequency morphologies, and subsequently reconstruct the background-free FLIM data. The lifetime components of

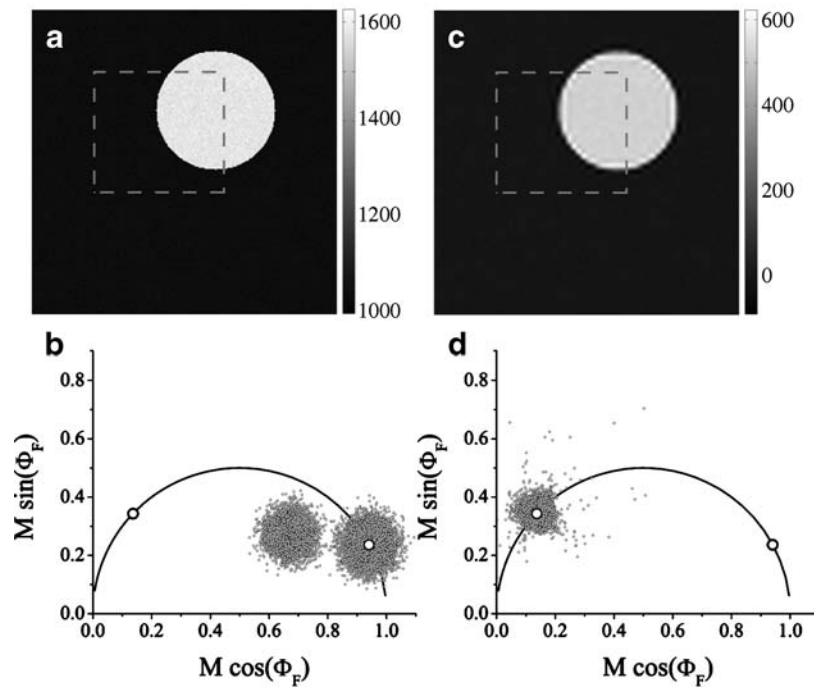


Fig. 6 The combination of wavelet analysis and FLIM with simulated data. The intensity images in (a) (before wavelet analysis) and (c) (after wavelet analysis) show two different morphologies: a region of interest (*small circle*) and a background (through out the entire image). (a and b) In the original data of (a) the background region contains a single lifetime of 1 ns and the small circle contains two lifetime components, a 10 ns component in addition to the 1 ns component. The dashed rectangle signifies pixels in the image that are fitted in the FLIM analysis, and plotted as a polar plot

in (b). In the polar plot of (b), the two open circles lying on the semicircle represent single lifetimes of 10 ns and 1 ns. See the text for a discussion. (c) Represents the results of the wavelet analysis on the data presented in (a) (see text for details of the simulation and the wavelet analysis). The polar plot of the FLIM analysis of the image in (c) is shown in (d). There is only one cluster of points on the polar plot centered on the point of 10 ns. This means the wavelet analysis has completely removed the background contribution

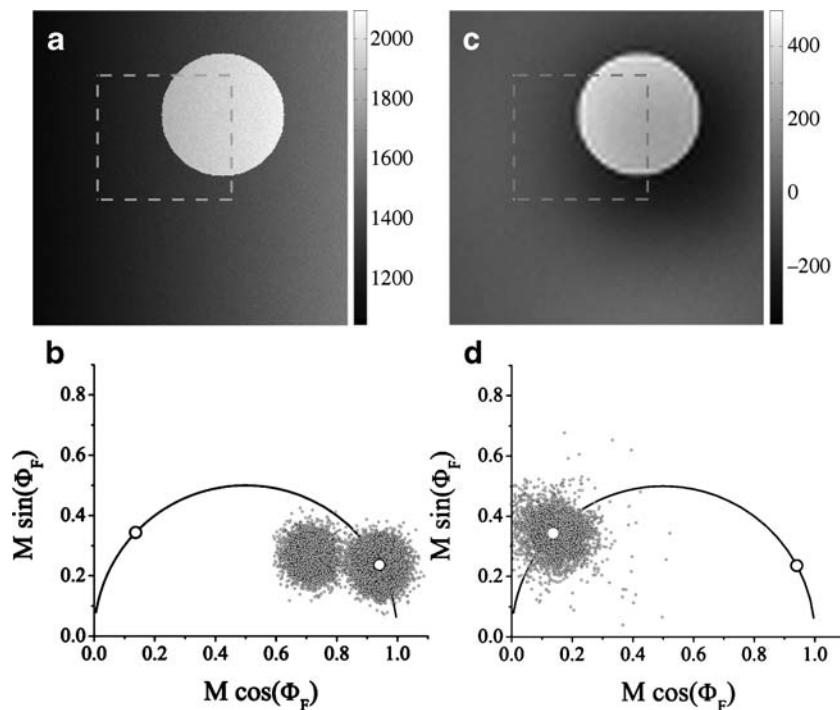


Fig. 7 The labeling of the sub-figures (a–d) are exactly as explained in the legend for Fig. 6. The background in this simulated data is increasing in amplitude with a constant gradient from left to right. The

wavelet analysis removes the background contribution from all the phase delay images, and therefore the recovery of the 10 ns single lifetime in the region of interest. See text

the background are removed from the region of interest as well. In Figs. 6 and 7, the analysis is performed on a simulated set of FLIM data. Then, in the next section, the same analysis is demonstrated on biological samples (Fig. 9).

Simulated data with constant background

Figure 6 is a fluorescence image from a set of homodyne FLIM simulated data. Eight phase delays with 10% random noise for a given pixel were simulated. A background signal with a single lifetime of 1 ns is evenly distributed throughout the whole region (big square). The region of interest (circle) contains a lifetime component with a 10 ns lifetime plus the 1 ns background component. The areas of the images that are analyzed with the FLIM algorithms to determine Φ_F and M at every pixel are highlighted by the dashed rectangle. From the data represented in Fig. 6a, two clusters of points are seen in the polar plot (Fig. 6b). The cluster located on the 1 ns point on the semicircle is from the background region inside the dashed rectangle, but outside the circle. The other cluster is centered on a straight line between the 1 and 10 ns points on the semicircle. The location of this cluster represents the combination of two lifetimes, 1 and 10 ns, inside the circle. The position on this straight line depends on the relative amplitudes of the two components [30].

Multi-resolution wavelet analysis (using the same set of functions discussed in Fig. 5) is then individually made with every phase-delayed original image. The difference between the images at approximation level 2 and level 10 is then reconstructed (Fig. 6c). Note that the background region is brought down to almost zero value because the low spatial frequencies beyond level 10 are removed altogether, leaving only the higher frequency components of the circle. The low spatial frequency components are removed from each of the eight phase-delayed images. The Φ_F and M values now form a single cluster on the polar plot centered at a location corresponding to 10 ns (Fig. 6d). Thus after this background subtraction, the 1 ns background component has been completely cancelled also in the circle and only the 10 ns component is left. This demonstrates that in FLIM, the wavelet analysis can play triple roles of selecting the region of interest, denoising and eliminating a background lifetime component simultaneously. The edges of the circle in the wavelet produced images are emphasized, but this does not affect the determination of the 10 ns Φ_F and M values (FLIM does not depend on the intensity). In this simulation the average of the background intensity is constant over the image, and if we knew the average value we could have just subtracted it without going through the wavelet analysis. However, it is often not possible to determine this average, and usually there is no good valid

background control. In the next section we simulate a varying background.

Simulated data with varying background

In Fig. 7 the same simulation and analysis are carried out, except the background is a linearly increasing gradient from left to right. The sub images (a,b,c and d) are constructed the same way as for Fig. 6. Again the wavelet analysis is able to select a spatial frequency band where the variable background component is suppressed, and the 10 ns lifetime component is extracted alone (Fig. 7d). In this case, without subtracting the background (Fig. 7a and b) the cluster from the mixture of 1 and 10 ns components (Fig. 7b) lies closer to the 1 ns intersection on the semicircle that in Fig. 6b because the fraction of the 1 ns component within the circle is larger than in Fig. 6b. But the background suppression is still excellent, showing the robustness of the wavelet procedure. This will work for any lifetime component where the local spatial frequencies are different than those of the region of interest by a sufficient amount. An obvious example is also elimination of high frequency noise (denoising).

The multi-step wavelet background removal on simulated FLIM data containing more than two lifetimes has been carried out with the same success in removing the background lifetime component, leaving the two lifetime components in the regions of interest, which can also be overlapping (data not shown).

Spinning disk FLIM with and without wavelets: application to dense bodies and M-lines in YFP transfected *Caenorhabditis elegans* live transformed cells

Using only spinning disk FLIM

The reduction of the out-of-focus background using the spinning disk confocal FLIM is tested in live cells where background fluorescence is abundant and not as simple as for Figs. 6 and 7. The samples are the transgenic nematode worm *C. elegans*. The samples were prepared as described in the thesis by Sophia Breusegem [51] except that we now use monomeric YFP and CFP rather than eYFP and eCFP. The main focus of this study is to identify the protein–protein interactions between PAT (Paralyzed and Arrested-elongation at Two-fold) proteins essential for muscle assembly in the body wall muscle cells of *C. elegans*. The PAT phenotype is found in the worms without the *pat* genes present resulting in the arrested in development when the worm reaches the two fold state during embryogenesis [52]. In the actual study of protein interaction monomeric CFP (the W7 variant with A206K mutation) is used as the FRET donor and the monomeric YFP (the 10C variant with

A206K mutation) is used as the FRET acceptor [51]. In the examples presented in Fig. 8, the transgenic worms carry only the PAT-4-mYFP fusion protein (that is, there is no hetero-FRET, and the lifetimes are not changed by possible FRET). Figure 8a and b are acquired without the spinning disk addition, and Fig. 8c and d are acquired with the spinning disk. It is known that the PAT-4 proteins are concentrated in the dense bodies and M-lines (bright spots). However, it is likely that there are some fluorescent proteins that are not localized in the either the dense bodies or in the M-lines. The extensive background fluorescence in Fig. 8a is probably due to non-localized PAT-4-mYFP, fluorescence originating from out-of-focus PAT-4-mYFP in

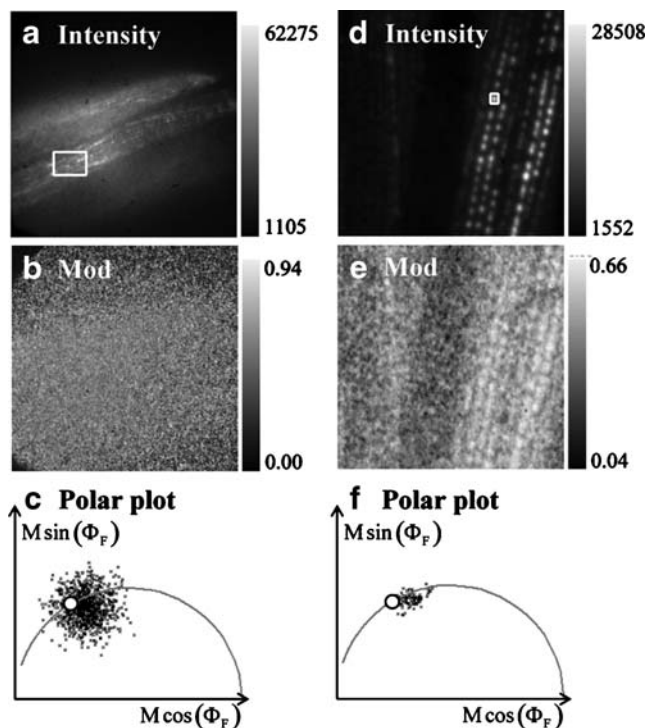


Fig. 8 A sample data set taken from a *C. elegans* carrying PAT-4-YFP protein fusion (see text), taken with a conventional full-field frequency-domain FLIM (a–c; left), and with the new setup with spinning disk confocal unit (d–f; right). Both instrumentation configurations show clear intensity images of muscle structure (a and d). The repeating pattern of bright spots is fluorescence from dense bodies. The M-lines are less visible. Regions of interest (open rectangles) containing muscle structure are shown in (a and d). The FLIM data from these images produce a cluster of points on the polar plot, (c and f), respectively. The open circles marked on the polar plot represent the reported value of approximately 2.9 ns of 10C YFP *in vivo* [53]. There is the possibility of having more than one lifetime components, because the point cluster is centered slightly inside the semicircle, but the major component will have a lifetime close to the reported value (see [30] for an in depth discussion of the polar plot). The muscle structure is obscured in the lifetime-resolved modulation image (b), which is due to contributions of out of focus fluorescence. On the other hand, the demodulation image from the data set taken using the spinning disk confocal FLIM arrangement (e) shows the similar distinct muscle structures seen in the intensity images

dense bodies, as well as background fluorescence from other intrinsic fluorophores. As one sees in the FLIM image, Fig. 8b, this out-of-focus fluorescence obscures the location of the dense bodies and M-lines. However, using the spinning disk confocal FLIM, the localization of the dense bodies and M-lines is accentuated in the intensity image Fig. 8d, and is visible in the FLIM image Fig. 8e. Therefore the spinning disk confocal FLIM setup helps distinguish fluorescence lifetimes originating from the dense bodies and M-lines from that of the background region.

The confocal FLIM measurement obtained from the spinning disk confocal unit greatly enhances the quality of the data and can be used in conjunction with the conventional method of using only pixels with intensities above a set threshold, or weighted averages of pixels, for the FLIM analysis. The variance of the polar plot points is also diminished (compare Fig. 8c and f) when using the spinning disk confocal attachment. This is a result of the confocal rejection of much of the out-of-focus fluorescence. Using the spinning disk, the improvement in signal-to-noise is obtained without compromising the speed of data acquisition. These lifetime images are derived from eight phase-sensitive intensity images obtained in eight seconds. Faster data acquisition is possible by either sacrificing signal-to-noise or higher fluorescence intensities. The fast acquisition time allows the use of FLIM to study the dynamics of interactions in live cells, such as the progress of protein–protein interactions over a course of cell development.

Applying wavelets before the analysis of spinning disk FLIM images

Figure 9 shows the result of applying a wavelet transformation to select fluorescence originating from the morphology corresponding to dense bodies, and to deselect background. The original data set (left, Fig. 9a and b) is taken from the spinning disk confocal setup. Fig. 9a is the original image, and Fig. 9c has undergone background discrimination by wavelet transformation. Both images have been subjected to a 10% thresholding (relative to the maximum values in each image). The center of the distributions within the polar plot clusters are indicated by the tips of the arrows (dashed arrow and dotted arrow correspond to the data before and after wavelet application, respectively). Depending on the relative values of the lifetimes of the background and sample, and their relative amplitudes, the fitted lifetime in the region of interest can be significantly falsified. The small clockwise movement of points along the semicircle for data subjected to the wavelet application (Fig. 9b) is due to the correct background subtraction of the wavelet procedure, which improves the accuracy of the FLIM analysis. The wavelets provide a

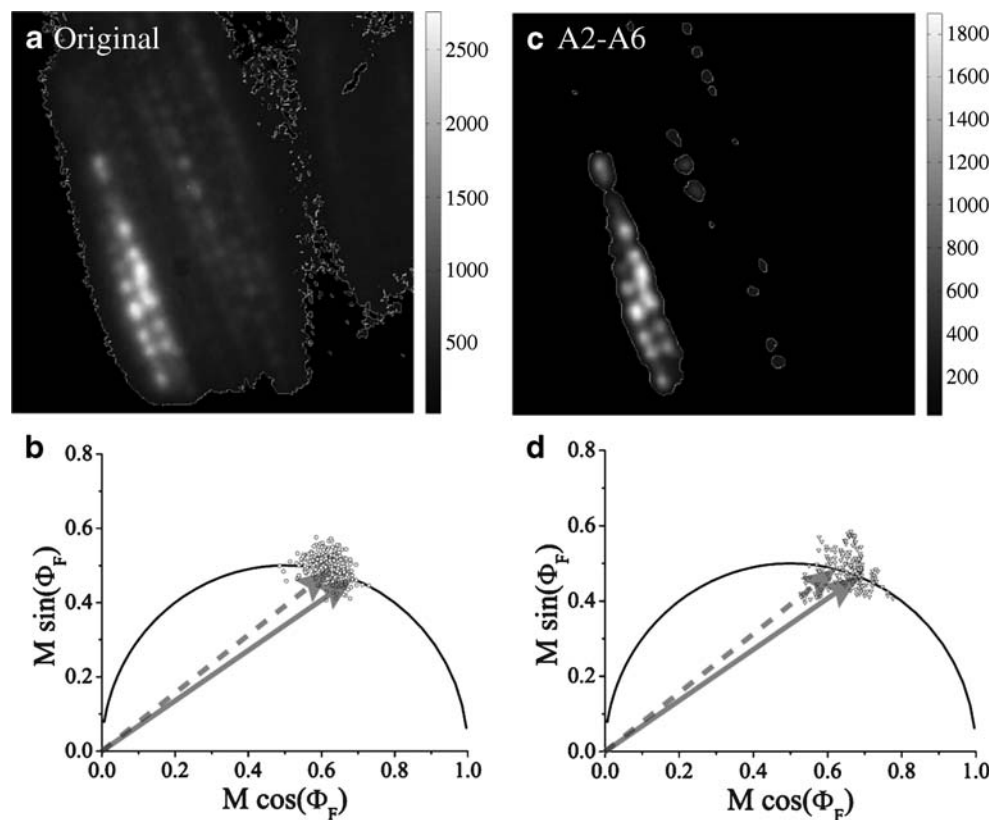


Fig. 9 The combination of wavelet analysis and FLIM. A *C. elegans* worm expressing PAT4-mCFP and PAT4-mYFP as FRET pair is measured with our spinning disk confocal FLIM setup (see text) with eight phase delay images. The original data set (left, **a** and **b**) is analyzed with our custom FLIM data analysis without any processing. For the edited data set (right, **c** and **d**), each phase-delay image is denoised and background subtracted using the wavelet method described previously. In case of the worm the difference between the approximation level 2 and level 6 is used. Then the analyzed phase-delay images are fitted to get the lifetime information. The intensity

images (**a** and **c**) are the average intensity images of the eight images. The highlighted regions in both images are those having intensity above 10% of the peak intensity. Obviously, the wavelet analysis facilitates the dense body and M-line selection. The polar plots (**b** and **d**) show lifetime information taken from the pixels having intensity above 50% of the peak intensities from the corresponding data. We believe that the slight shift to the faster time of the analyzed data on the polar plot, from the tip of the dashed arrow to the tip of the solid arrow, is due to the removal of the contribution from the background lifetime component

valuable way to correct for background contributions, which could falsify lifetime determinations, especially for complex biological samples.

Conclusion

We have incorporated a spinning disk confocal unit into our conventional full-field frequency-domain FLIM instrument. This extends our real-time FLIM instrumentation from 2-D with background interference to 3-D with suppressed out-of-focus background interference. We have also presented a new method of suppressing background by using wavelets for emphasizing morphological features of the images before undertaking the analysis of the modulation and phase. This procedure also removes the background lifetime component from the regions of interest. This wavelet procedure is particularly convenient when measuring FLIM in the

frequency domain with homodyne techniques. We have used this instrumentation for FLIM measurements in live cells and/or thick tissues where both data acquisition speed and the out-of-focus background fluorescence are critical concerns. Preliminary data using our spinning disk FLIM exhibits new features of interest in the lifetime images, of a transgenic nematode *C. elegans* and a fruit fly *D. melanogaster* larva which would have been concealed under the out-of-focus background fluorescence in case of a conventional full-field FLIM setup. The data acquisition speed is only slightly compromised due to the lower signal. The analysis of each acquired plane takes the same time as a non-confocal image. Moreover, in a case where regions of interest are localized or highly structured as shown in our examples, the local character of a “wavelet transform” can pick out the relevant features of the targeted locations. This is also an excellent way to decrease the background fluorescence, and it works well with our FLIM analysis.

Acknowledgments We thank Glen Redford for his valuable contributions to the non-confocal version of the frequency domain full field FLIM, and his original work on the polar plot. We appreciate discussions with Bryan Spring about wavelets. The work presented here has been partially supported by the NIH grant (PHS 5 P41 RRO3155) and by start-up funds from the UIUC Physics Department (RMC).

the image intensifier S_{ave} (Eq. 4 of text) is derived, following Schneider et al. [36] as

$$S_{avg} = \langle F(t) \cdot D(t) \rangle = \frac{1}{T} \int_0^T (F_0 + F \cdot \cos(\omega t - \Phi_E - \Phi_F)) \cdot (D_0 + D \cdot \cos(\omega t - \Phi_D)) dt \tag{A1}$$

Supplementary data

In the case of the conventional wide field frequency-domain lifetime imaging, the homodyne signal recorded at

$$S_{avg} = \frac{1}{T} \left[\int_0^T F_0 \cdot D_0 dt + \frac{1}{2} \int_0^T F \cdot D \cdot \cos(\Delta\Phi_{DE} - \Phi_F) dt + \frac{1}{2} \int_0^T F \cdot D \cdot \cos(2\omega t - \Delta\Phi_{DE} - \Phi_F) dt + \int_0^T F_0 \cdot D \cdot \cos(\omega t - \Phi_D) dt + \int_0^T D_0 \cdot F \cdot \cos(\omega t - \Phi_E - \Phi_F) dt \right] \tag{A2}$$

When T is large compared with $1/\omega$, as in our case, the last three terms in Eq. A2 vanish due to averaging. Therefore,

In the case of the spinning disk confocal FLIM, the fluorescence signal emitted is switching between the bright period and the dark period and can be written as in Eq. A4

$$S_{avg} = F_0 \cdot D_0 + \frac{F \cdot D}{2} \cdot \cos(\Delta\Phi_{DE} - \Phi_F) = S_0 \left(1 + \frac{M}{2} \cdot \cos(\Delta\Phi_{DE} - \Phi_F) \right) \tag{A3}$$

$$F(t) = \begin{cases} F_0 + F \cdot \cos(\omega t - \Phi_E - \Phi_F) & \text{when } n \cdot T_D \leq t \leq n \cdot T_D + T_B; n = 0, 1, \dots, T/(T_D + T_B) \\ 0 & \text{otherwise} \end{cases} \tag{A4}$$

By putting Eq. A4 back into Eq. A1 and carrying out the calculation proves that this switching behavior reduces the total signal collected by the image intensifier but does not affect the final form of the homodyne signal, i.e. Eq. A3 above is still valid.

References

1. Cundall RB, Dale RE (1983) Time-resolved fluorescence spectroscopy in biochemistry and biology, in NATO ASI series. Series A, Life sciences, vol. 69, F. NATO Advanced Study Institute on Time-Resolved Fluorescence Spectroscopy in Biochemistry and Biology (1980: Saint Andrews, Ed. New York: Plenum, p. 785

2. Lakowicz JR (1999) Principles of fluorescence spectroscopy, 2nd edn. Kluwer/Plenum , New York
3. Gadella TWJ, Jovin TM, Clegg RM (1993) Fluorescence lifetime imaging microscopy (FLIM): Spatial resolution of microstructures on the nanosecond time scale. Biophys Chemist 48:221–239
4. Szmajcinski H, Lakowicz JR (1995) Possibility of simultaneously measuring low and high calcium concentrations using Fura-2 and lifetime-based sensing. Cell Calcium 18:64–75
5. Zhong W, Urayama P, Mycek MA (2003) Imaging fluorescence lifetime modulation of a ruthenium-based dye in living cells: the potential for oxygen sensing. J Phys D: Appl Phys 36:1689–1695
6. Clegg RM, Holub O, Gohlke C (2003) Fluorescence lifetime-resolved imaging: measuring lifetimes in an image. Methods Enzymol 360:509–542
7. van Munster EB, Gadella TWJ (2005) Fluorescence Lifetime Imaging Microscopy (FLIM). Adv Biochem Eng Biotechnol 95:143–175

8. Suhling K, French PMW, Phillips D (2005) Time-resolved fluorescence microscopy. *Photochem Photobiol Sci* 4:13–22
9. Clegg RM, Schneider PC (1996) In: Slavik J (ed) *Fluorescence microscopy and fluorescent probes*. Plenum, New York, pp 15–33
10. Redford GI, Clegg RM (2005) In: Periasamy A, Day RN (eds) *Molecular imaging: FRET microscopy and spectroscopy*. Oxford University Press, New York, pp 193–226
11. Becker W (2005) *Advanced time-correlated single photon counting techniques*, in Springer Series in Chemical Physics. Springer, vol 81, p. 401
12. Marriott G, Clegg RM, Arndt-Jovin DJ, Jovin TM (1991) Time resolved imaging microscopy. *Phosphorescence and delayed fluorescence imaging*. *Biophys J* 60(6):1374–1387
13. Cubeddu R, Taroni P, Valentini G, Canti G (1991) Use of time-gated fluorescence imaging for diagnosis in biomedicine. *J Photochem Photobiol, B Biol* 12:109–113
14. Cubeddu R, Comelli D, D'Andrea C, Taroni P, Valentini G (2002) Time-resolved fluorescence imaging in biology and medicine. *J Phys, D, Appl Phys* 35:R61–R76
15. Gratton E, Breusegem S, Sutin JRQ, Barry NP (2003) Fluorescence lifetime imaging for the two-photon microscope: time-domain and frequency-domain methods. *J of Biomedical Optics* 8 (3):381–390
16. Sytsma, Vroom, Grauw d, Gerritsen (1998) Time-gated fluorescence lifetime imaging and microvolume spectroscopy using two-photon excitation. *J Microsc* 191(1):39–51
17. Buurman JM, Knutson JR, Ross JBA, Turner BW, Brand L (1992) Fluorescence lifetime imaging using a confocal laser scanning microscope. *Scanning* 14:155–159
18. Piston DW, Sandison DR, Webb WW (1992) Time-resolved fluorescence imaging and background rejection by two-photon excitation in laser scanning microscopy. *Proc. SPIE* 1604, (Time-resolved Laser Spectroscopy in Biochemistry III), 379–389
19. Hanson KM, Behne MJ, Barry NP, Mauro TM, Gratton E, Clegg RM (2002) Two-photon fluorescence lifetime imaging of the skin stratum corneum pH gradient. *Biophys J* 83(3):1682–1690
20. Ghiggino KP, Harris MR, Spizzirri PG (1992) Fluorescence lifetime measurements using a novel fiber-optic laser scanning confocal microscope. *Rev Sci Instrum* 63(5):2999–3002
21. Patterson GH, Piston DW (2000) Photobleaching in two-photon excitation microscopy. *Biophys J* 78:2159–2162
22. Buranachai C, Clegg RM (2008) In: Rothnagel J (ed) *Fluorescent proteins: methods and applications*. Humana, pp (in press)
23. van Munster EB, Goedhart J, Kremers GJ, Manders EMM, Gadella TWJ Jr (2007) Combination of a spinning disc confocal unit with frequency-domain fluorescence lifetime imaging microscopy. *Cytometry Part A* 71A:207–214
24. Kawamura S, Negishi H, Otsuki S, Tomosada N (2002) Confocal laser microscope scanner and CCD camera. *Yokogawa Technical Report English Edition* 33:17–33
25. Nakano A (2002) Spinning-disk confocal microscopy—A cutting-edge tool for imaging of membrane traffic. *Cell Struct Funct* 27 (5):349–355
26. Graf R, Rietdorf J, Zimmermann T (2005) Live cell spinning disk microscopy. *Adv Biochem Eng Biotechnol* 95:57–75
27. Inoue S, Inoue T (2002) Direct-view high-speed confocal scanner: The CSU-10. *Methods Cell Biol* 70:87
28. Wang E, Babbey CM, Dunn KW (2005) Performance comparison between the high-speed Yokogawa spinning disc confocal system and single-point scanning confocal systems. *J Microsc* 218:148–159
29. Clayton AHA, Hanley QS, Vermeer PJ (2004) Graphical representation and multicomponent analysis of single-frequency fluorescence lifetime imaging microscopy data. *J Microsc* 213(1):1–5
30. Redford GI, Clegg RM (2005) Polar plot representation for frequency-domain analysis of fluorescence lifetimes. *J Fluoresc* 15(5):805–815
31. Holub O, Seufferheld MJ, Gohlke C, Govindjee, Heiss GJ, Clegg RM (2007) Fluorescence lifetime imaging microscopy of *Chlamydomonas reinhardtii*: non-photochemical quenching mutants and the effect of photosynthetic inhibitors on the slow chlorophyll fluorescence transients. *J Microsc* 226(2):90–120
32. Cole KS, Cole RH (1941) Dispersion and absorption in dielectrics. *J Chem Phys* 9:341
33. von Hippel AR (1954) *Dielectrics and waves*. Wiley, New York, p xii
34. Hill NE, Vaughan WE, Price AH, Davies M (1969) *Dielectric properties and molecular behavior*. van Nostrand, New York
35. Sjöback R, Nygren J, Kubista M (1995) Absorption and fluorescence properties of fluorescein. *Spectrochim Acta, Part A* 51:L7–L21
36. Schneider PC, Clegg RM (1997) Rapid acquisition, analysis, and display of fluorescence lifetime-resolved images for real-time applications. *Rev Sci Instrum* 68(11):4107–4119
37. Mallat SG (1989) A theory for multiresolution signal decomposition: The wavelet representation. *IEEE Trans Pattern Anal Mach Intell* 11(7):674–693
38. Starck JL, Murtagh F, Bijaoui A (1998) *Image processing and data analysis*. Cambridge University Press, Cambridge
39. Starck JL, Bijaoui A (1994) Filtering and deconvolution by the wavelet transform. *Signal Processing* 35:195–211
40. Nowak RD, Baraniuk RG (1999) Wavelet-domain filtering for photon imaging systems. *IEEE Trans Image process* 8(5):666–678
41. Boutet de Monvel J, Le Calvez S, Ulfendahl M (2001) Image restoration for confocal microscopy: improving the limits of deconvolution, with application to the visualization of the mammalian hearing organ. *Biophys J* 80:2455–2470
42. Shapiro JM (1991) Embedded image coding using zerotrees of wavelet coefficients. *IEEE Trans Signal Process* 41(12):3445–3462
43. Grgic S, Grgic M, Zovko-Cihlar B (2001) Performance analysis of image compression using wavelets. *IEEE Trans Ind Electron* 48 (3):682–695
44. Bernas T, Asem EK, Robinson JP, Rajwa B (2006) Compression of fluorescence microscopy images based on the signal-to-noise estimation. *Microsc Res Tech* 69:1–9
45. Olivo-Marin J-C (2002) Extraction of spots in biological images using multiscale products. *Pattern Recogn* 35:1989–1996
46. Willett RM, Nowak RD (2003) Platelets: a multiscale approach for recovering edges and surfaces in photon-limited medical imaging. *IEEE Trans Med Imag* 22(3):332–350
47. Genovesio A, Liedl T, Emiliani V, Parak WJ, Coppey-Moisan M, Olivo-Marin J-C (2006) Multiple particle tracking in 3-D+ t microscopy: method and application to the tracking of endocytosed quantum dots. *IEEE Trans Image Process* 15(5):1062–1070
48. Walker JS (1997) Fourier analysis and wavelet analysis. *Notices of the AMS* 44(6):658–670
49. Hong L (1993) Multi-resolutional filtering using wavelet transform. *IEEE Trans Aerosp Electron Syst* 29(4):1244–1251
50. Petrou M, Bostdogianni P (1999) *Image processing: the fundamentals*. Wiley, New York
51. Breusegem SY (2002) In vivo investigation of protein interactions in *C. elegans* by Foerster Resonance Energy Transfer Microscopy, In *Biophysics And Computational Biology*. Urbana-Champaign: University of Illinois, p 216
52. Williams BD, Waterston RH (1994) Genes critical for muscle development and function in *Caenorhabditis elegans* identified through lethal mutations. *J Cell Biol* 124:475–490
53. Pepperkok R, Squire A, Geley S, Bastiaens PIH (1999) Simultaneous detection of multiple green fluorescent proteins in live cells by fluorescence lifetime imaging microscopy. *Curr Biol* 9(5):269–272